Membraneless Unbuffered Seawater Electrolysis for Pure Hydrogen Production

Nan-Nan Liang
　Kyungpook National University

Hyunwoong Park (✉ hwp@knu.ac.kr)
　Kyungpook National University　https://orcid.org/0000-0002-4938-6907

Article

Membraneless Unbuffered Seawater Electrolysis for Pure Hydrogen Production

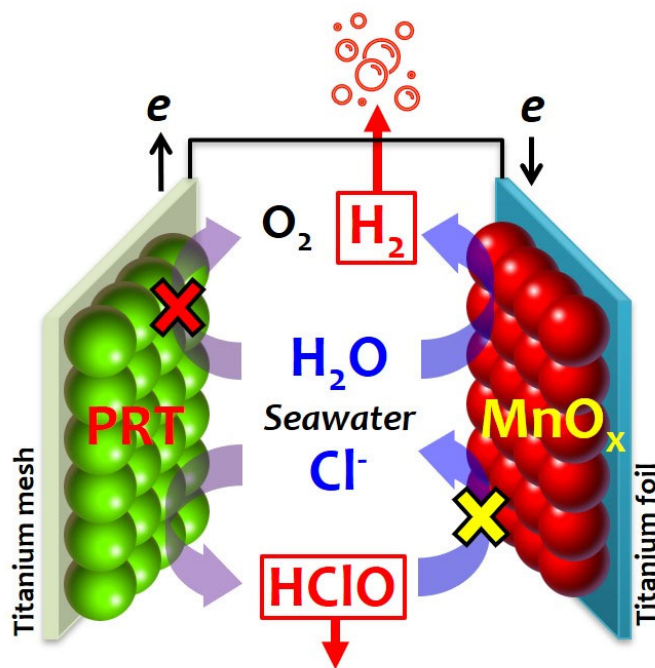Nan-Nan Liang and Hyunwoong Park*

School of Energy Engineering, Kyungpook National University, Daegu 41566, Republic of Korea

*To whom correspondence should be addressed:

Tel: +82-53-950-8973; E-mail: hwp@knu.ac.kr

Broader Context

Electrolytic hydrogen production is considered a key energy transition, carbon-neutral technology when coupled with renewable energy production processes. As the H_2 price is highly dependent on geographic location, the maritime transport of as-produced H_2 at low costs to locations where the H_2 production is unfavorable is an alternative. In this regard, seawater electrolysis is promising for *in situ* H_2 production and overseas transport. Although the conventional electrolysis has been extensively studied in well-defined aqueous environment characteristics (e.g., electrolyte and pH), such conditions cannot be directly applied to the seawater electrolysis at a pH ~8.2 because of the presence of several types of natural inorganic species. Conventional seawater electrolysis proceeds under alkaline conditions (pH > 13) to ensure the selectivity of the oxygen evolution reaction (OER) over the chloride oxidation reaction (ClOR). In addition, membranes are required to inhibit the chlorine reduction reaction (ClRR) at the cathode and maximize the hydrogen evolution reaction (HER) while separating H_2 from O_2. Herein, we propose a novel membraneless electrolysis process for the production of high-purity H_2 from unperturbed, unbuffered seawater at pH 8.2. To achieve this goal, we attempted to synthesize ClOR-selective anodes and ClRR-inhibitive cathodes, while completely retarding the OER at the anode and maximizing the HER at the cathode. The as-synthesized anode and cathode pair drove ClOR and HER with Faradaic efficiencies of ~100% over 100 h in a single-compartment cell containing seawater at pH 8.2. This technology is expected to enable *in situ* seawater electrolysis to produce high-purity H_2, which can be quickly collected and transported overseas.

Abstract

Seawater electrolysis is promising as an *in situ* H_2 production method, allowing immediate overseas transport of the produced H_2. Typically, it proceeds under alkaline conditions to ensure the selectivity of the oxygen evolution reaction (OER) over the chloride oxidation reaction (ClOR). In addition, electrolyzers usually require membranes to inhibit the chlorine reduction reaction (ClRR) and maximize the hydrogen evolution reaction (HER) while separating H_2 from O_2. In this study, membraneless electrolysis of undisturbed, unbuffered seawater (pH 8.2) is proposed to produce high-purity H_2. A ternary component catalyst with Pt, Ru, and Ti (PRT) and a minimized Pt level ($Pt_{0.06}Ru_{0.24}Ti_{0.7}O_x$) drives ClOR at a Faradaic efficiency (FE) of ~100% in saline water at an industrial level of current density ($J = 800$ mA cm^{-2}) over 500 h. ClRR is also inhibited on MnO_x electrodes, leading to ~100% FE of H_2 production even in the presence of chlorines ($HClO/ClO^-$). Finally, the PRT anode/MnO_x cathode pair drive ClOR and HER at FEs of ~100% at $J = 80$ mA cm^{-2} over 100 h in a single-compartment cell containing seawater. Moreover, the OER and ClRR are completely inhibited during seawater electrolysis.

Introduction

Electrolytic hydrogen production is considered a key energy transition, carbon-neutral technology when coupled with renewable energy production processes.[1-9] The minimum H_2 production cost was estimated to decrease from \$4.56 kg^{-1} in 2020 to \$2.44 kg^{-1} in 2050 upon direct connection with solar- and wind-powered grids.[10,11] As the H_2 price is highly dependent on geographic location, the maritime transport of as-produced H_2 at low costs to locations where the H_2 production is unfavorable is an alternative. In this regard, seawater electrolysis is promising for *in situ* H_2 production and overseas transport. Harvesting renewable energy and directly connecting it to the electrolyzer further increases the technical readiness of seawater electrolysis.[4,12,13]

Although the conventional electrolysis has been extensively studied in well-defined aqueous environment characteristics (e.g., electrolyte and pH), such conditions cannot be directly applied to the seawater electrolysis at a pH ~8.2 because of the presence of several types of natural inorganic species.[6,14-17] Among them, chlorides seriously interfere with oxygen and hydrogen evolution reactions (OER and HER, respectively).[7,18,19] The electrochemical potentials of chloride oxidation reaction (ClOR, reaction 1 at $E° = 1.482$ V) and OER ($E° = 1.229$ V) are similar, but the ClOR with two-electron transfer becomes dominant,[20-23] particularly at high current densities. In addition, the chlorine reduction reaction (ClRR, a reverse of ClOR) with the as-produced chlorines (represented by the $HClO/ClO^-$ pair, $pK_a = 7.46$) competes with HER.[8,9,19,22-24] The active involvement of ClOR/ClRR eventually reduces the Faradaic efficiencies (FEs) of O_2 and H_2 production.

$$Cl^- + H_2O \leftrightarrow HClO + H^+ + 2\,e^- \tag{1}$$

To address this challenge, a membraned alkaline electrolysis system has often been employed for seawater electrolysis.[14,25,26] An increase in the pH of seawater reduces both $E°_{OER}$ and $E°_{ClOR}$ to different degrees (e.g., $E°_{OER}$ = 0.401 V and $E°_{ClOR}$ = 0.81 at pH 14), and the OER becomes dominant over the ClOR.[26,27] Even if ClOR occurs concurrently, the employed membranes separate evolved O_2 and H_2 gases as well as inhibit the crossover of HClO to the catholyte. Accordingly, the negative effects of ClOR/ClRR are minimized. Although feasible, however, the synthesis of OER-selective catalyst durably working at a large J in seawater is difficult. In addition, the use of membranes and corrosive KOH significantly increases the H_2 production cost.[28,29] Furthermore, dissolved organic substances (~90% of the total organic carbon in the oceans) interfere with the OER and cause fouling of the membranes.[30,31]

With this in mind, we propose a membraneless electrolysis of unperturbed, unbuffered seawater at pH 8.2 for the production of high-purity H_2. To achieve this goal, we attempted to synthesize ClOR-selective anodes and ClRR-inhibitive cathodes, while completely retarding the OER at the anode and maximizing the HER at the cathode (**Scheme 1**). If the ClOR and HER are coupled, high-purity H_2 gas without O_2 can be obtained with no need of a membrane because the as-formed chlorines remain in the aqueous phase. For selective ClOR and HER, ternary Pt, Ru, and Ti oxide (PRT) anodes and MnO_x cathodes were synthesized, respectively. An optimized PRT electrocatalyst with a minimized Pt level ($Pt_{0.06}Ru_{0.24}Ti_{0.7}O_x$) drove ClOR at an FE of ~100% in saline water at an industrial level of J (0.8 A cm^{-2}) over 500 h. Furthermore, ClRR was effectively inhibited by the MnO_x cathode, leading to ~100% FE in the H_2 production. Finally, the PRT anode and MnO_x cathode pair produced aqueous free chlorine and H_2 gas with FEs of ~100% over 100 h in a single-compartment cell containing

5

seawater at pH 8.2.
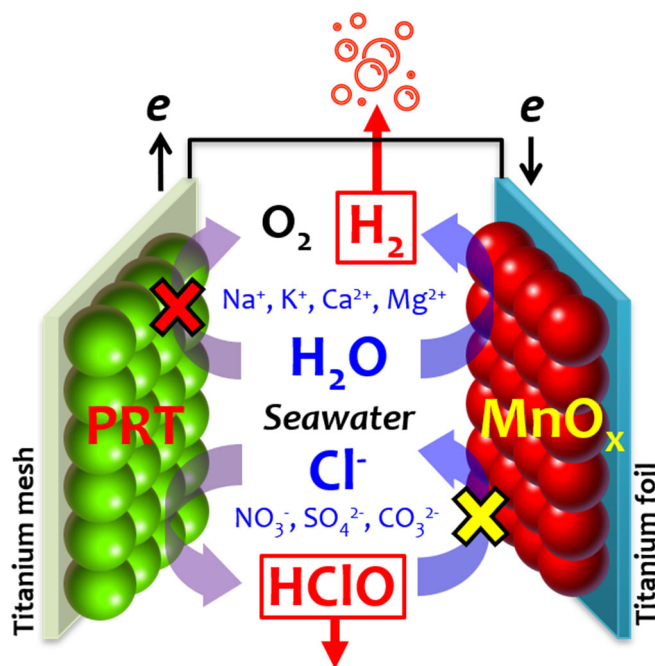
Scheme 1. Illustration of seawater electrolysis with a Pt, Ru, and Ti (PRT) anode and MnO_x cathode pair in a membraneless single-compartment cell. Conventional seawater electrolysis proceeds under alkaline conditions (pH > 13) to secure selectivity of oxygen evolution reaction (OER) over chloride oxidation reaction (ClOR). In addition, it usually requires membranes to inhibit chlorine reduction reaction (ClRR) and maximize hydrogen evolution reaction (HER), while separating H_2 from O_2. However, if the electrolysis products are only HClO (and/or ClO^-) in solution and H_2 in headspace at Faradaic efficiencies of ~100% for ClOR and HER, respectively, membranes for separating gases (H_2 from O_2) and inhibiting chlorine reduction at the cathode are not necessary.

Experimental

Synthesis and surface characterization of materials

Analytical grade chemical reagents and solvents were purchased from Sigma-Aldrich and used without further purification, unless otherwise mentioned. Titanium meshes (1 cm × 3 cm, 1-mm thick, Alfa Aesar) and foils (0.127-mm thick, 99.7% pure, Aldrich) were rubbed with sand paper, washed with deionized water (18 MΩ cm) and ethanol, and subsequently treated with aqueous HCl (37%) solution for 20 min at 50 °C. In sequence, the substrates were washed with excess deionized water and ethanol. For the synthesis of ternary $(Pt_{0.2}Ru_{0.8})_xTi_{1-x}O_y$ (PRT-x) particles ($x = 0.1$–0.4), various ratios of $H_2PtCl_6 \cdot H_2O$ (dissolved in 0.1 mL HCl), $RuCl_3 \cdot H_2O$ (dissolved in 0.1 mL HCl), and $Ti(C_4H_9O)_4$ (dissolved in 0.5 mL ethanol) were mixed in a mixed solution of citric acid ($C_6H_8O_7$, Duksan, 99.5%) and ethylene glycol ($C_2H_6O_2$, Daejung, 99.5%) (1/4 by molar ratio) at 90 °C. After mixing for 5 min, the PRT samples were annealed at various temperatures (400–900°C) for 1 h in air. The as-obtained PRT powder (10 mg) was dispersed in 2-propanol (2 mL, C_3H_8O, Duksan, 99.9%) using ultrasound for 2 h. This PRT slurry was sprayed onto Ti meshes with an air gun at loading masses of 0.83–3.33 mg cm^{-2}. Subsequently, the PRT/Ti samples were dried overnight in air. Unless otherwise specified, PRT represents the sample for $x = 0.3$ (i.e., $Pt_{0.06}Ru_{0.24}Ti_{0.7}O_y$) annealed at 500 °C with a loading mass of 3.33 mg cm^{-2}. For comparison, binary $Pt_{0.2}Ru_{0.8}O_y$ (PR, *i.e.*, PRT with $x = 1$) was synthesized at 500 °C for 1 h in air.

For the MnO_x electrodes, a $Mn(NO_3)_2$ (>97%) solution (2 M, dissolved in 10 μL ethanol) was evenly dispersed over the Ti foil using a short-haired brush. The electrode samples were dried at 60 °C for 10 min and annealed at various temperatures (200–500 °C) for 10 min in air.

7

This brushing-annealing cycle was repeated to load different masses of MnO_x ($1-10$ mg cm^{-2}). After the final cycle, the electrodes were additionally annealed for 1 h. Unless otherwise specified, MnO_x was annealed at 400 °C with a loading mass of 7 mg cm^{-2}.

The surface morphologies of the as-synthesized samples (particles and/or electrodes) were analyzed by scanning electron microscopy (SEM, Su-8230, Hitachi) at an accelerating voltage of 5.0 kV. A high-resolution field-emission transmission electron microscope (HR-FE-TEM, JEOL, JEM-2100F) equipped with energy-dispersive spectroscopy (EDS, X-MaxN80, Horiba) was employed at an accelerating voltage of 200 kV. The surface areas of the powders were determined using the Brunauer–Emmett–Teller (BET; Micrometrics, ASAP 2020) method with N_2 as the adsorbate gas. X-ray diffraction (XRD, PANalytical EMPUREAN) with Cu-Kα radiation (40 kV and 30 mA) and X-ray photoelectron spectroscopy (XPS, Thermo Fisher Scientific) with Al-Kα (hν = 1486.6 eV) were performed to examine the crystalline patterns and elemental states of the as-synthesized samples, respectively.

Electrochemical activity tests and characterization

Linear sweep voltammograms of the as-synthesized electrodes (working electrodes) were obtained at a scan rate of 5 mV s^{-1} with a saturated calomel electrode (SCE, reference electrode) and Pt wire (counter electrode) using an electrochemical workstation (Ivium) in aqueous saline solutions with various compositions at pH 6 ($0.0137-0.941$ M NaCl, 0.5 M NaCl with 5 mM NaClO, and 0.4 M NaCl with 100 mM NaClO) or artificial seawater (Instant Ocean, salinity 36 g L^{-1}) at pH 8.2. $NaClO_4$ ($0.0137-0.5$ M) was used instead of NaCl to examine the chloride effect where necessary. For bulk electrolysis, the as-synthesized PRT or MnO_x electrodes were

held at constant J values (10–800 mA cm^{-2}) in saline and seawater solutions in a single-compartment cell or two-compartment cell divided with a cation exchange membrane (CEM, CMI-7000S, Membranes International) (open or sealed to the atmosphere) while recording the electrode potentials (E) with respect to the SCE. When the PRT and MnO$_x$ were coupled as the anode and cathode, respectively, a constant cell J (J_{cell}) of 80 mA cm^{-2} was applied, and the resulting cell voltage (E_{cell}) was recorded using a direct current power supply (Agilent E3633A). During the bulk electrolysis, the solution was intermittently sampled and the free chlorines (represented by HClO/ClO$^-$) were quantified using the N,N-diethyl-p-phenylenediamine reagent by the Hach method, as described elsewhere.[15-17,32,33] The evolved gases in the cell headspace were also analyzed for O$_2$ and H$_2$ using a gas chromatograph (GC, Agilent 7820A; Inficon Micro GC Fusion) equipped with dual flame ionization and thermal conductivity detectors. For *in situ*, real-time analysis of O$_2$ and H$_2$ gases during prolonged bulk electrolysis over 100 h, the PRT anode/ MnO$_x$ cathode pair at a distance of 30 mm was placed in an air-tight single-compartment cell through which N$_2$-sparged seawater (pH 8.2) continuously flowed at a rate of 11 mL min^{-1} using a peristaltic pump (BT100-2J-19). During electrolysis, evolved gases with high-purity N$_2$ carrier gas (>99.99%) flowed through the headspace of the cell at a rate of 20 mL min^{-1} and entered into a quadrupole mass spectrometer (Quality Mass Spectrometer, Hiden, GB/QIC-20). The composition of the headspace O$_2$ and H$_2$ gases was calibrated using standard gases. Simultaneously, free chlorine in the electrolyzed seawater was analyzed.

The electrochemical impedance spectroscopy of the as-synthesized PRT and MnO$_x$ electrodes was conducted at 1.1 and -1.5 V vs. SCE in the frequency ranges of 100 kHz to

0.1 Hz and 50 kHz to 0.01 Hz, respectively, with an amplitude of 10 mV. The double-layer capacitance values of the electrodes proportional to the electrochemically active surface area were also examined by cyclic voltammetry in the E ranges of 0.85 to 0.95 V vs. SCE and −0.2 to −0.1 V vs. SCE, respectively, at varying scan rates in the range 20–100 mV s^{-1}. The Faradaic efficiencies (FEs) for the ClOR, ClRR, HER, and OER were estimated using the following equation:

$$FE\ (\%) = [\Delta P_c \times n_c \times F \times 100\%] / (J \times t)$$

where ΔP_c, n_c, F, and t refer to the amount (mol) of compounds produced (HClO, H$_2$, and O$_2$) or consumed (HClO), stoichiometric number of such compounds ($n_c = 2$ for HClO and H$_2$; $n_c = 4$ for O$_2$), Faraday constant (96,486 C mol^{-1}), and time (s), respectively. Hereafter, SCE is omitted for working electrodes with half-reactions, unless otherwise mentioned.

Results and discussion

Achieving high efficiency ClOR with durable PRT electrodes

The crystalline structures of the as-synthesized binary PR (Pt$_{0.2}$Ru$_{0.8}$O$_y$) and ternary PRT (PRT-0.3) particles were examined (**Fig. 1a**). The PR sample (annealed at 500 °C) exhibited characteristic diffraction patterns of metallic Pt (PDF no. 04-0802 with 2θ = 39.76°, 46.23°, 67.45°, 81.29°, and 85.71° for (111), (200), (220), (311), and (222), respectively) and RuO$_2$ (PDF no. 40-1290 with 2θ = 28.01°, 35.05°, 40.02°, 40.06°, and 54.25° for (110), (101), (200), (111), and (211), respectively). Traces of metallic Ru peaks were also found at 2θ = 42.15° (002) and 44.01° (101) (PDF no. 06-0663), which disappeared upon oxidative annealing at a higher temperature (**Fig. S1**). The PRT sample annealed at 500 °C displayed a mixture of RuO$_2$

and rutile TiO_2 (PDF no. 21-1276 with $2\theta = 27.45°$, $36.09°$, 41.23, $54.32°$, $56.64°$, and $69.01°$ for (110), (101), (111), (211), (220), and (301), respectively), along with Pt diffraction peaks.
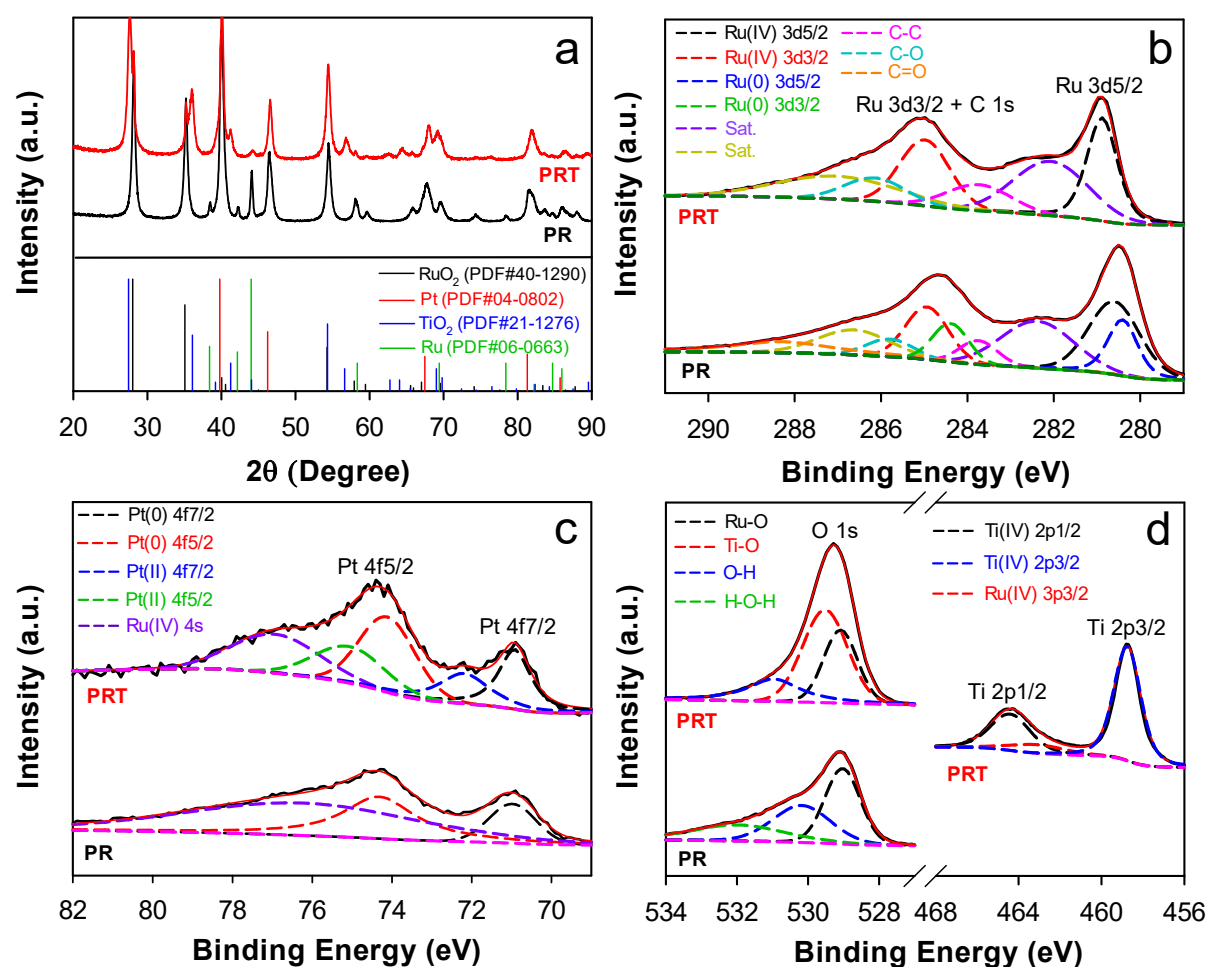

Figure 1. Surface characterization of as-synthesized binary PR ($Pt_{0.2}Ru_{0.8}O_y$) and ternary PRT ($Pt_{0.06}Ru_{0.24}Ti_{0.7}O_y$) particles annealed at 500 °C. (a) XRD spectra. (b-d) XPS spectra (b: Ru 3d, c: Pt 4f, and d: Ti 2p and O 1s). Deconvoluted XPS spectra are shown as dashed lines

The XPS spectra further revealed the elemental states of the as-synthesized PR and PRT particles (**Fig. 1b–1d**). For both samples, the Ru 3d spectra showed the spin-orbit doublet at binding energies of 280.9 eV (Ru $3d_{5/2}$) and 285 eV (Ru $3d_{3/2}$) (**Fig. 1b**). The Ru $3d_{3/2}$ band appeared to be mixed with the C 1s band, which was attributed to intrinsic or adsorbed carbon impurities. This was confirmed by the C 1s band observed for the PR sample annealed at 800 °C

11

(**Fig. S2**). Notably, the binding energy of the Ru 3d bands with the PRT sample was higher than that of the PR sample by 0.4 eV, owing to the dominant Ru^{4+} species and absence of Ru^{0} in the PRT sample. The Pt 4f bands in the PRT sample were located at 70.9 eV (Pt $4f_{7/2}$) and 74.6 eV (Pt $4f_{5/2}$), and the deconvolution of the bands revealed the coexistence of Pt^{0} and Pt^{2+} (**Fig. 1c**). In contrast, only Pt^{0} was found in the PR sample, and Pt^{2+} species were formed upon calcination at a high temperature (800 °C) (**Fig. S2**). The broad shoulder bands at ~76.4 eV were attributed to the Ru^{4+} 4s band. This suggests that TiO_2 facilitated the oxidation of Ru^{3+} and Pt^{0} to Ru^{4+} and Pt^{2+}, respectively, during the oxidative annealing process at 500 °C. Moreover, the shifts in the Ru 3d and Pt 4f bands upon the introduction of TiO_2 indicate strong interactions between Ru and Pt with TiO_2. The Ti 2p band of the PRT sample also shows the characteristic doublet spectra of $2p_{3/2}$ (458.8 eV) and $2p_{1/2}$ (464.3 eV), attributed to the Ti^{4+} species (**Fig. 1d**). The contribution of the Ru $3p_{3/2}$ band was observed in the deconvoluted Ti 2p band. Finally, the O 1s bands of the PR and PRT samples were compared. The deconvoluted three sub-bands in the PR sample were assigned to lattice oxygen (Ru-O-Ru at 529.1 eV), surface oxygen (Ru-OH at 530.2 eV), and adsorbed oxygen (e.g., H_2O at 532.1 eV).[34] Although an additional lattice oxygen (Ti-O-Ti at 529.7 eV) was found in the PRT sample, the contribution of the adsorbed oxygen was negligible.
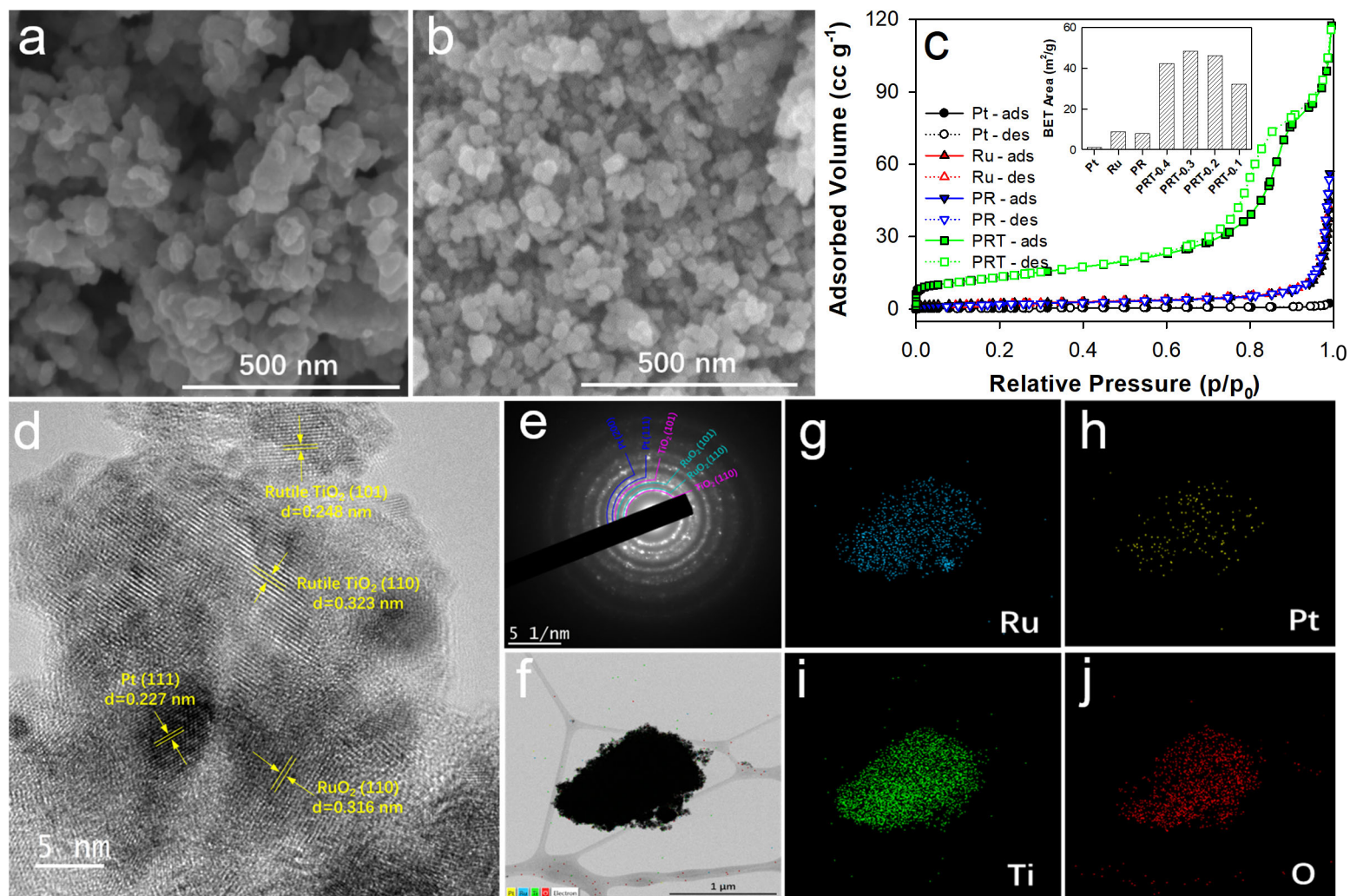
Figure 2. (a and b) SEM images of as-synthesized PR and PRT particles, respectively. (c) Isotherm N_2 adsorption-desorption curves with the as-synthesized Pt, RuO_2, PR, and PRT samples. Inset shows BET surface areas. (d and e) HR-TEM image and SAED pattern of the PRT sample. (f–j) EDS and elemental mappings of the PRT sample.

The as-synthesized PR sample was composed of irregularly shaped particles (**Fig. 2a**), and the primary particle size increased with the annealing temperature (**Fig. S3**). In contrast, the PRT sample displayed a relatively uniform spherical configuration with an average diameter of ~27 nm (**Fig. 2b**). The isotherm N_2 adsorption-desorption curves indicated a negligible interaction of N_2 with Pt, whereas N_2 adsorption was enhanced with Ru (and consequently PR) (**Fig. 2c**). Notably, the PRT sample exhibited a significantly high adsorption capacity with hysteresis (**Fig. S4**), indicating a mesoporous structure. The BET areas with PRT were large (>40 $m^2 g^{-1}$), whereas the other samples exhibited areas of <10 $m^2 g^{-1}$ (**Fig. 2c inset**). The HR-TEM analysis of the PRT sample showed aggregates with primary particles of 10–20 nm (**Fig. S5**). Magnified HR-TEM images further revealed mixed interplanar spacings of 0.248 and 0.323 nm corresponding to the (101) and (110) planes of rutile TiO_2, respectively, 0.316 nm corresponding to the (110) plane of RuO_2, and 0.227 nm corresponding to the (111) plane of Pt (**Fig. 2d**). These crystalline planes were intimately connected to each other, forming strong interfacial contacts. The selected area electron diffraction (SAED) pattern further confirmed the coexistence of ternary crystalline structures with TiO_2, RuO_2, and Pt (**Fig. 2e**), which is in good agreement with the XRD and HR-TEM images. The EDS and elemental mapping analysis clearly showed a uniform distribution of Ru, Pt, Ti, and O; however, the Pt signal was weak owing to the low Pt content (~6%) (**Fig. 2f–2j**).

The as-synthesized binary PR and ternary PRT particles were sprayed onto Ti meshes, and the electrochemical behavior of the as-sprayed electrodes was examined in NaCl and $NaClO_4$ electrolytes. The linear sweep voltammograms with the PR electrode showed an onset potential (E_{on}) value of ~0.95 V in both electrolytes, whereas a larger J was obtained in the NaCl

electrolyte (**Fig. 3a**). A similar tendency was also observed with single Ru (i.e., RuO_2) and Pt electrodes; however, the Pt electrode was nearly inactive in both solutions. The ternary PRT followed the same tendency, but the voltammogram difference between NaCl and $NaClO_4$ was significant. In the NaCl solution, the optimal PR fraction was found to be 0.3 (i.e., PRT-0.3 or $Pt_{0.06}Ru_{0.24}Ti_{0.7}O_y$), beyond which the electrochemical activity decreased (**Fig. S6**). Considering that OER is the primary oxidation reaction in a chloride-free solution (i.e., $NaClO_4$), whereas a combination of ClOR and OER can occur in a chloride solution, an enhanced J value with NaCl may indicate that ClOR was favored over OER with PR and more significantly with PRT.

To quantitatively compare the ClOR efficiency, bulk electrolysis with various electrodes at $J = 80$ mA cm^{-2} was performed (**Fig. 3b**). In 0.5 M NaCl, free chlorine (i.e., HClO/ClO$^-$) was linearly produced with time (**Fig. 3b inset**), maintaining a ClOR-FE value of ~100% with the PRT electrode. This FE value was higher than that with the PR electrode (~84%), although the molar amounts of Pt and Ru in the PRT electrode were only 30% of those in the PR electrode. Moreover, Pt and Ru exhibited considerably lower ClOR-FE values (<60%). As the electrolyte concentration decreased to 0.137 and 0.0137 M, respectively, the voltammogram difference with PRT between NaCl and $NaClO_4$ gradually reduced (**Fig. S7**). Nevertheless, ~100% ClOR-FE with PRT was obtained in 0.137 M NaCl. When the loading amount of PRT (3.33 mg cm^{-2}) was reduced by 75% (0.83 mg cm^{-2}; denoted as PRT (1/4)), E_{on} increased by +0.08 V and E increased to 0.5 V for $J = 80$ mA cm^{-2}. This larger E value was attributed to the reduced active surface area of the catalysts.
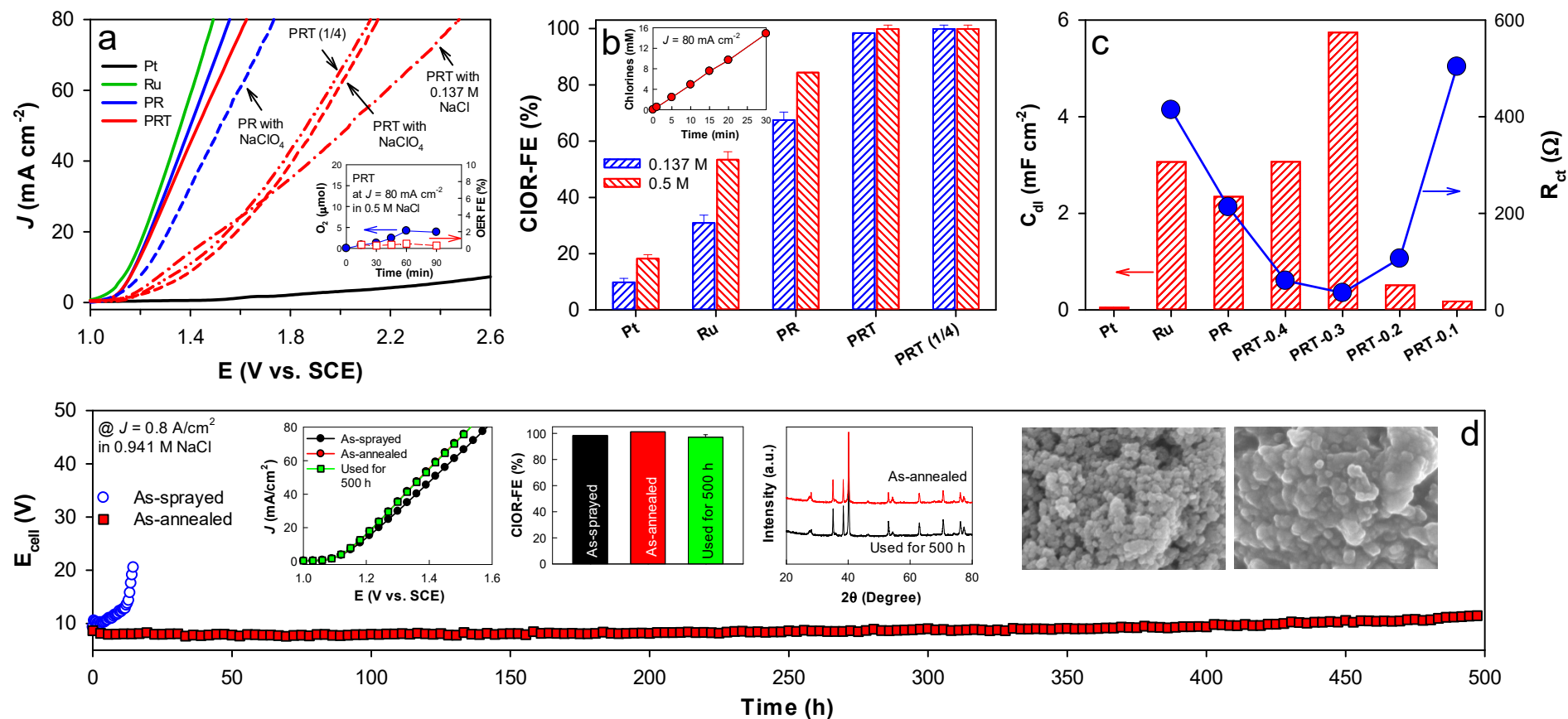
Figure 3. (a) Linear sweep voltammograms with Pt, Ru, PR, and PRT electrodes in 0.5 M NaCl solutions at pH 6. For comparison, 0.137 M NaCl or 0.5 M NaClO$_4$ (pH 6) were also used. PRT (1/4) refers to the PRT with loading mass of 0.83 mg cm^{-2}. The inset shows the O$_2$ evolution and its FE with PRT at J = 80 mA cm^{-2} in 0.5 M NaCl. (b) FE values of ClOR at J = 80 mA cm^{-2}. The inset shows the free chlorine production with time at J = 80 mA cm^{-2}. (c) C$_{dl}$ and R$_{ct}$ values. (d) Prolonged electrolysis with the as-sprayed and as-annealed PRT anodes at J = 800 mA cm^{-2} in 0.941 M NaCl. Insets show voltammograms and FE values (at J = 80 mA cm^{-2}) of the as-sprayed, as-annealed, and 500 h-used PRT electrodes in 0.5 M NaCl solutions. XRD spectra and SEM images (left: as-annealed, right: used for 500 h) are also shown.

16

For example, the masses of the Pt and Ru salts with PRT (1/4) decreased to 0.073 and 0.135 mg cm^{-2}, respectively. Nevertheless, ~100% ClOR-FE was achieved with PRT (1/4) (**Fig. 3b**). Under the same electrolysis conditions, the OER with PRT was remarkably inhibited with an FE of <1% (**Fig. 3a inset**). These results indicate that the as-synthesized PRT was highly selective for ClOR.

The electrocatalytic activity of the as-synthesized electrodes is associated with the electrochemical active surface area, which is proportional to the double-layer capacitance (C_{dl}). The C_{dl} value for PRT-0.3 was estimated to be ~5.7 mF cm^{-2}, which was higher than the values for single and binary composition electrodes (0.05, 3.1, and 2.3 mF cm^{-2} for Pt, Ru, and PR, respectively) and also the values for other ternary PRT electrodes (**Figs. 3c and S8**). C_{dl} appeared to be influenced by oxides (TiO_2 and RuO_2) and was maximized at $x = 0.3$. PRT-0.3 also exhibited the lowest interfacial charge-transfer resistance (R_{ct}) (**Fig. S9**). Electrochemical impedance spectroscopic analysis revealed that PRT-3 had the smallest R_{ct} value (35.7 Ω) among the PRT series. The single and binary electrodes exhibited large R_{ct} values (Pt: 2700 Ω, Ru: 414 Ω, PR: 213 Ω). These results partly explain the superior activity of PRT-0.3 compared to that of all other single, binary, and ternary compositions.

The stability of the optimized PRT electrode was examined under severe conditions ($J = 800$ mA cm^{-2}; 0.941 M NaCl) while recording E_{cell} of the PRT anode and the mesh-type Ti cathode pair (**Fig. 3d**). E_{cell} was 10.5 V in the initial stage and abruptly increased to >20 V at ~10 h. The PRT particles immobilized on the substrate (Ti mesh) via a spray process readily peeled off from the substrate after 10 h. Hence, the as-sprayed PRT electrode was annealed at 300 °C for 6 h to induce robust contact, and its stability was tested again. The initial value of

17

E_{cell} (8.5 V) was maintained over 400 h, and only slightly increased to ~11 V after 500 h. The voltammograms of the annealed PRT electrodes (before and after 500 h of electrolysis) were the same, whereas their J values were larger than those of the as-sprayed PRT, which was attributed to the enhanced contact of the catalysts with the substrate upon annealing (**Fig. 3d inset**). The ClOR-FE value of the 500 h-used PRT electrode was ~97%, which was nearly the same as that of the as-annealed electrode. In addition, the crystalline structure (XRD in **Fig. 3d inset**) and elemental states (XPS in **Fig. S10**) did not change after 500 h of electrolysis. However, the catalyst surface appeared to melt, and the particles became aggregated (SEM in **Fig. 3d inset**). This phenomenon of interparticle fusion is typical.[34-36] Nevertheless, the as-observed electrocatalytic activity and stability were outstanding compared to those obtained in previous reports (**Table S1**).

Inhibiting ClRR with MnO$_x$ electrodes

For suppression of the ClRR, MnO$_x$ electrodes were synthesized at various temperatures. The MnO$_x$ electrode synthesized at 200 ºC (MnO$_x$-200) demonstrated an inhomogeneous cracked morphology, whereas compact uniform particles were observed in the MnO$_x$-400 sample (**Fig. S11**). The XRD spectra of both samples exhibited the same diffraction patterns corresponding to Mn$_2$O$_3$ (PDF no. 24-0508; $2\theta = 23.12°$, 32.92°, 38.20, 45.14°, 49.32°, 55.14°, and 65.72° for the (211), (222), (400), (323), (413), (044), and (622) planes, respectively) (**Fig. 4a and S12**). The HR-TEM images of the MnO$_x$-400 sample demonstrated an interplanar spacing of 0.2714 nm, corresponding to the (222) plane of Mn$_2$O$_3$ (**Fig. 4b**). XPS analysis was performed to examine the Mn valence states of both samples (**Fig. 4c**).
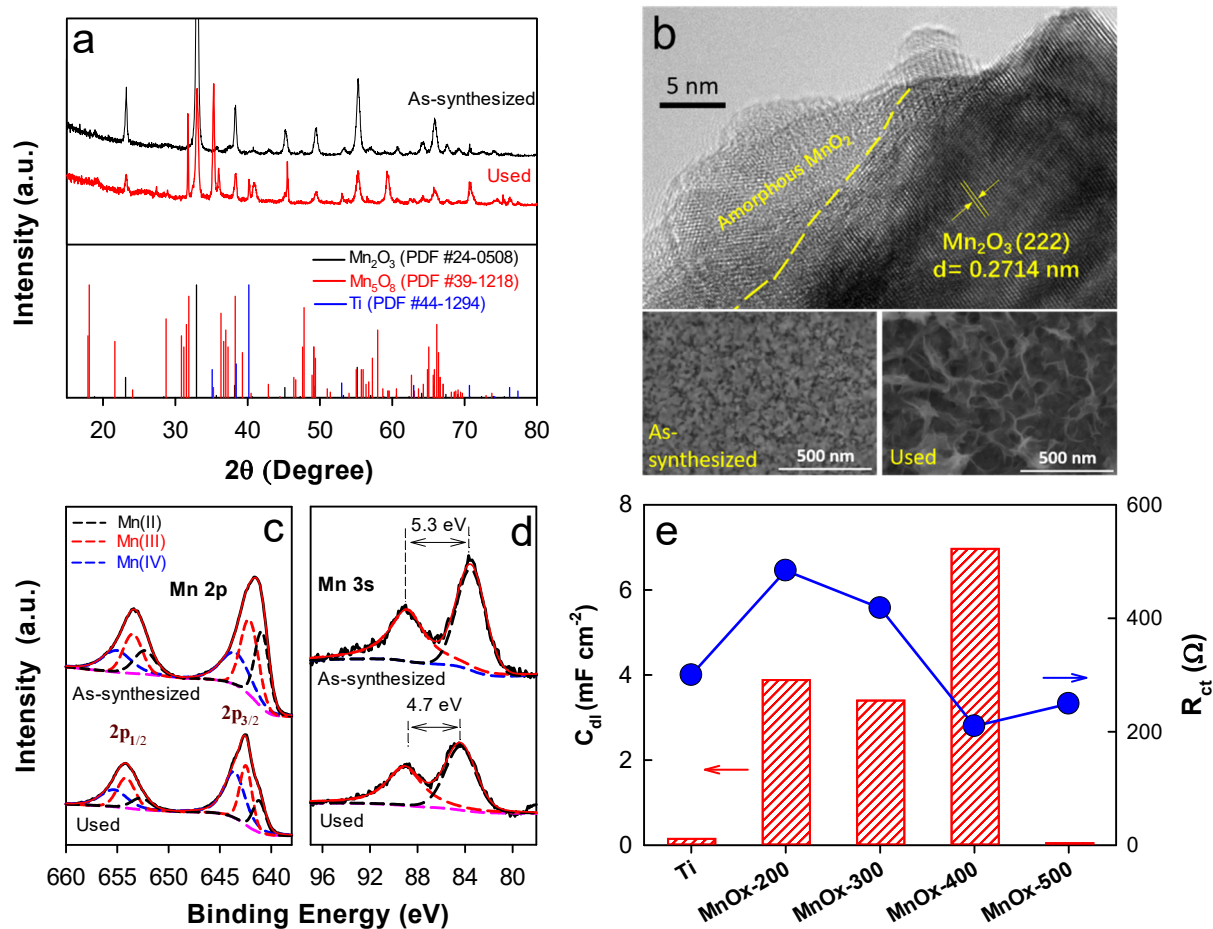
Figure 4. Surface and electrochemical analysis of MnO$_x$ electrodes (deposited on Ti plates) annealed at various temperatures (200–500 °C). Unless otherwise specified, MnO$_x$ stands for MnO$_x$-400 (annealed at 400 °C). (a) XRD spectra, (b) HR-TEM and SEM images (top and bottom panels, respectively), (c and d) XPS spectra (Mn 2p and Mn 3s, respectively), and (e) C$_{dl}$ and R$_{ct}$. After 100 h of electrolysis, the used MnO$_x$ samples were also examined with XRD, SEM, and XPS.

The Mn 2p bands (2p$_{1/2}$ and 2p$_{3/2}$ at binding energies of 653.4 eV and 641.6 eV, respectively) in both samples appeared similar, and the deconvolution of the bands with MnO$_x$-400 revealed mixed Mn(II), Mn(III), and Mn(IV) sub-bands at fractions of 30%, 37%, and 33%, respectively (31%, 39%, and 30% for MnO$_x$-200, respectively). The binding energy differences between the two Mn 3s bands were estimated to be 5.2 eV and 5.3 eV, respectively (**Fig. 4d**). This indicated that the average oxidation states of the surface Mn atoms were ~3.1 and ~3.0 for

19

MnO$_x$-200 and MnO$_x$-400, respectively.[37,38] The as-synthesized MnO$_x$ electrodes exhibited various C$_{dl}$ and R$_{ct}$ values depending on the annealing temperature (**Fig. 4e**). Among the samples, MnO$_x$-400 showed the highest C$_{dl}$ value (6.97 mF cm^{-2}) and the lowest R$_{ct}$ value (209 Ω) (**Fig. S13** and **S14**). MnO$_x$-200 demonstrated the second highest C$_{dl}$ (3.89 mF cm^{-2}) but the worst R$_{ct}$. The C$_{dl}$ of MnO$_x$-500 was as small as that of the Ti substrate, but the R$_{ct}$ value was comparable to that of MnO$_x$-400.

The electrocatalytic activities of the as-synthesized MnO$_x$ electrodes (deposited on a Ti plate) were examined for the ClRR and HER in NaCl solutions (with and without NaClO). The voltammograms of MnO$_x$-400 indicated an E_{on} of *approximately* −1.8 V (corresponding to −1.2 V vs. reversible hydrogen electrode (RHE)), regardless of the presence of NaClO (**Fig. 5a**). This indicates a negligible ClRR with HClO/ClO$^-$. In contrast, the Ti plate (without MnO$_x$ catalysts) exhibited an E_{on} of *approximately* −1.7 V (corresponding to −1.1 V vs. RHE) in a 0.5 M NaCl solution. The voltammogram gradually shifted to a positive potential in the presence of 5 mM and 100 mM NaClO, with E_{on} values of −1.6 and −1.4 V, respectively. Notably, two distinct reduction peaks were observed at −0.55 V and −1.04 V with 100 mM NaClO due to the ClRR.[39,40] For comparison, voltammograms with Pt electrodes were also examined. E_{on} with a Pt electrode exhibited a more positive value than the corresponding values with Ti and MnO$_x$ in the NaCl solution. In addition, the voltammogram shifted to a positive potential in the presence of NaClO, and ClRR peaks were observed. These behaviors indicate that Pt should also be active in the ClRR. Bulk electrolysis for the ClRR was further performed using 5 mM NaClO (**Fig. 5b**). For the Pt and Ti substrates at $J = -10$ mA cm^{-2}, the concentrations of chlorine (C$_t$ / C$_0$) linearly decreased with time with a ClRR-FE of 18–20%.
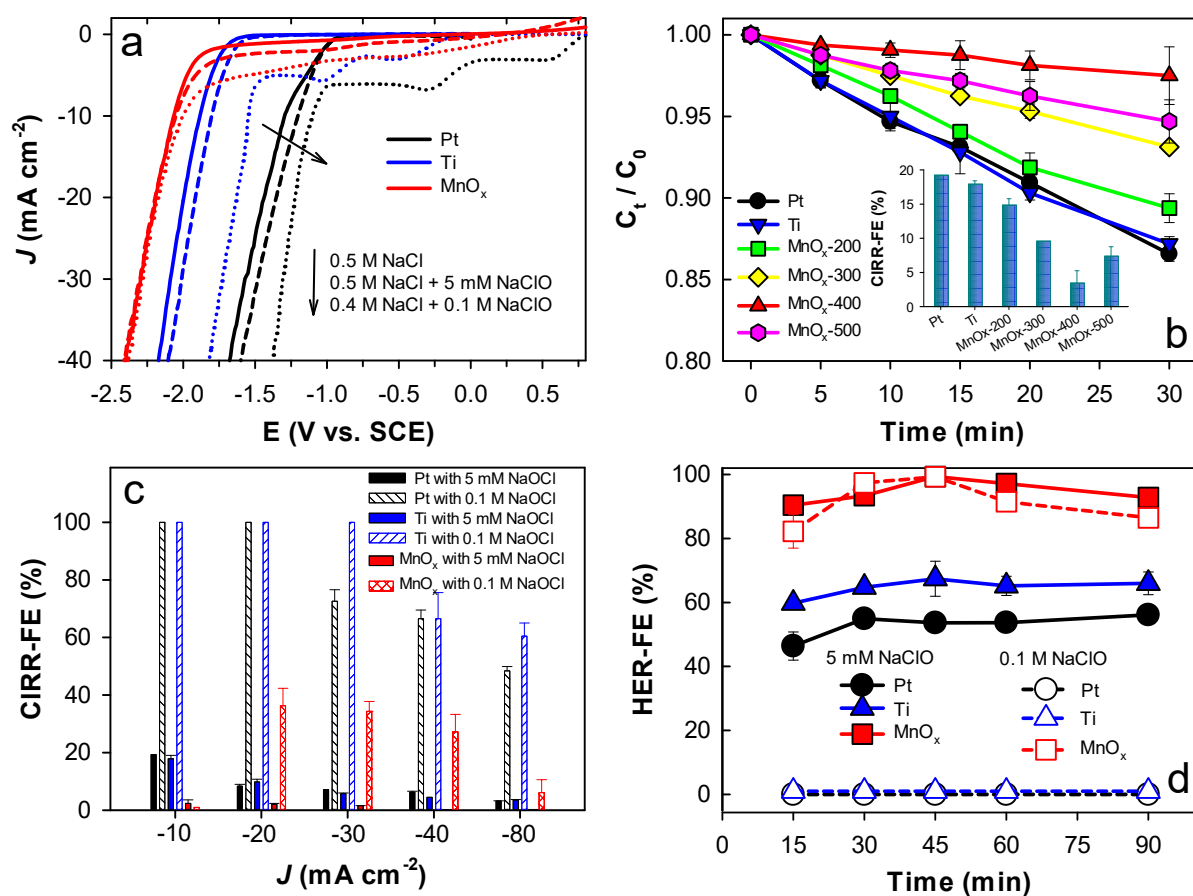
Figure 5. Electrochemical behavior and activities for ClRR and HER with Pt, Ti, and MnOx electrodes in 0.5 M NaCl, 0.5 M NaCl with 5 mM NaClO, or 0.4 M NaCl with 0.1 M NaClO solutions at pH 6. Unless otherwise specified, MnOx stands for MnOx-400 (annealed at 400 °C). (a) Linear sweep voltammograms. (b) Changes in the concentration of chlorines (C_t / C_0) with various electrodes at $J = -10$ mA cm^{-2} in 0.5 M NaCl with 5 mM NaClO in a two-compartment cell divided by a CEM. The inset shows ClRR-FE values in 30 min. (c) ClRR-FE values as a function of J and NaOCl concentration. (d) HER-FE changes at $J = -10$ mA cm^{-2} in 0.5 M NaCl with 5 mM NaClO.

This decrease in chlorine concentration was significantly inhibited by the MnOx electrodes. Among them, MnOx-400 required the smallest E value at $J = -10$ mA cm^{-2} (**Fig. S15**), with a ClRR-FE of approximately 3% (**Fig. 5b inset**). The ClRR typically proceeds with HClO/ClO$^-$ adsorption, followed by breaking of the Cl–O bond, Cl adsorption with concurrent H$_2$O release, and Cl$^-$ release.[41] Considering that the isoelectric point of MnOx was located at pH < ~4 (**Fig. S16**),[42] the HClO/ClO$^-$ access should be inhibited to the negatively charged MnOx surface at a

circumneutral pH value.[24]

The ClRR-FE was significantly influenced by the type of electrode, NaClO concentration, and J value (**Fig. 5c**). For the Ti substrate with 5 mM NaClO, the ClRR-FE value gradually decreased with increasing J because of the concurrent HER. With 100 mM NaClO, the ClRR-FEs with the Ti were ~100% at $J \leq -30$ mA cm^{-2} and decreased to ~65% at larger J values. A similar behavior was observed for Pt, albeit with lower ClRR-FE values than those for Ti at $J \geq -30$ mA cm^{-2} with 100 mM NaClO. This indicates that the HER occurred more efficiently with Pt than with Ti, particularly at high concentrations of NaClO. In contrast, the ClRR-FEs with MnO$_x$ were <3% at all the tested J values with 5 mM NaClO. With 100 mM NaClO, a volcanic ClRR-FE profile was obtained by blocking the HClO access at a low J and by a competitive HER at a high J. MnO$_x$, Ti, and Pt electrodes produced H$_2$ in NaCl solutions with 5 mM NaClO at $J = -10$ mA cm^{-2}, leading to HER-FEs of >90%, ~65%, and ~55%, respectively (**Fig. 5d**). When the NaClO concentration increased to 100 mM, no H$_2$ was evolved with Ti and Pt (hence, zero HER-FEs). However, nearly the same amounts of H$_2$ were produced with MnO$_x$ with 5 mM and 100 mM NaClO (hence, similar HER-FEs). These results confirm that MnO$_x$ is highly selective for the HER in saline water containing chlorines.

The stability of the as-synthesized MnO$_x$ electrode was further tested over 100 h at $J = -10$ mA cm^{-2} and -80 mA cm^{-2} in 0.5 M NaCl solutions. E values of approximately -3.5 V and -4.2 V, respectively, were maintained over 100 h (**Fig. S17**). The used MnO$_x$ electrode with $J = -10$ mA cm^{-2} for 100 h exhibited new crystalline structures originating from Mn$_5$O$_8$ (**Fig. 4a**). The particle-compact surface also changed into an unfolded tissue-like surface (**Fig. 4b**). A deconvolution of the Mn 2p bands further revealed a fractional ratio of 17/32/51 for

Mn(II)/Mn(III)/Mn(IV) (**Fig. 4c**), whereas the average oxidation state of the Mn atom increased from 3.0 to ~3.7 (**Fig. 4d**). Despite the cathodic reaction, this increase in the oxidation state can be attributed to the hypochlorite-mediated partial oxidation of MnO_x.[24]

Membraneless seawater electrolysis and production of pure H$_2$ gas

The as-synthesized PRT and MnO_x electrodes were wired in a membraneless single-compartment cell containing seawater at a pH of 8.2. The E_{on} values in the anodic and cathodic voltammograms were slightly different from those in 0.5 M NaCl at pH 6 (**Fig. 6a**), likely owing to different pH values and composition.[43] The voltammograms further indicated that an anode/cathode cell potential (E_{cell}) of ~4.8 V (= 1.8 V – (–3 V)) was required for $J_{cell} = 80$ mA cm^{-2}. Under galvanostatic conditions at $J_{cell} = 80$ mA cm^{-2}, chlorine was linearly produced with a ClOR-FE of ~100% (**Fig. 6b**). This FE value was the same as that obtained for the two-compartment cell equipped with a membrane (**Fig. 3**). When MnO_x was replaced with a Ti plate, the ClER-FE gradually decreased to ~80% owing to the concurrent ClRR with the Ti plate. This ClRR should compete with the HER, thereby lowering the HER-FE to ~80% (**Fig. 6c**). In contrast, an HER-FE of ~100% was obtained with the PRT/MnO_x pair.

Prolonged electrolysis of seawater was conducted in a continuous-flow, membraneless reactor equipped with a PRT/MnO_x pair (**Fig. 6d**). The headspace gases were monitored *in situ* in real time using a quadrupole mass spectrometer. At $J_{cell} = 80$ mA cm^{-2}, an E_{cell} of ~4.8 V was stably maintained over 100 h, whereas ClOR occurred at an FE of ~100%, and the OER-FE was <0.5% (virtually zero). H$_2$ gas was continuously produced with an FE of approximately 100%. No changes in the E_{cell} and FE values were observed during electrolysis. These results

23

clearly indicate that the PRT/MnO$_x$ pair is effective in producing high-purity H$_2$ gas via membraneless seawater electrolysis.
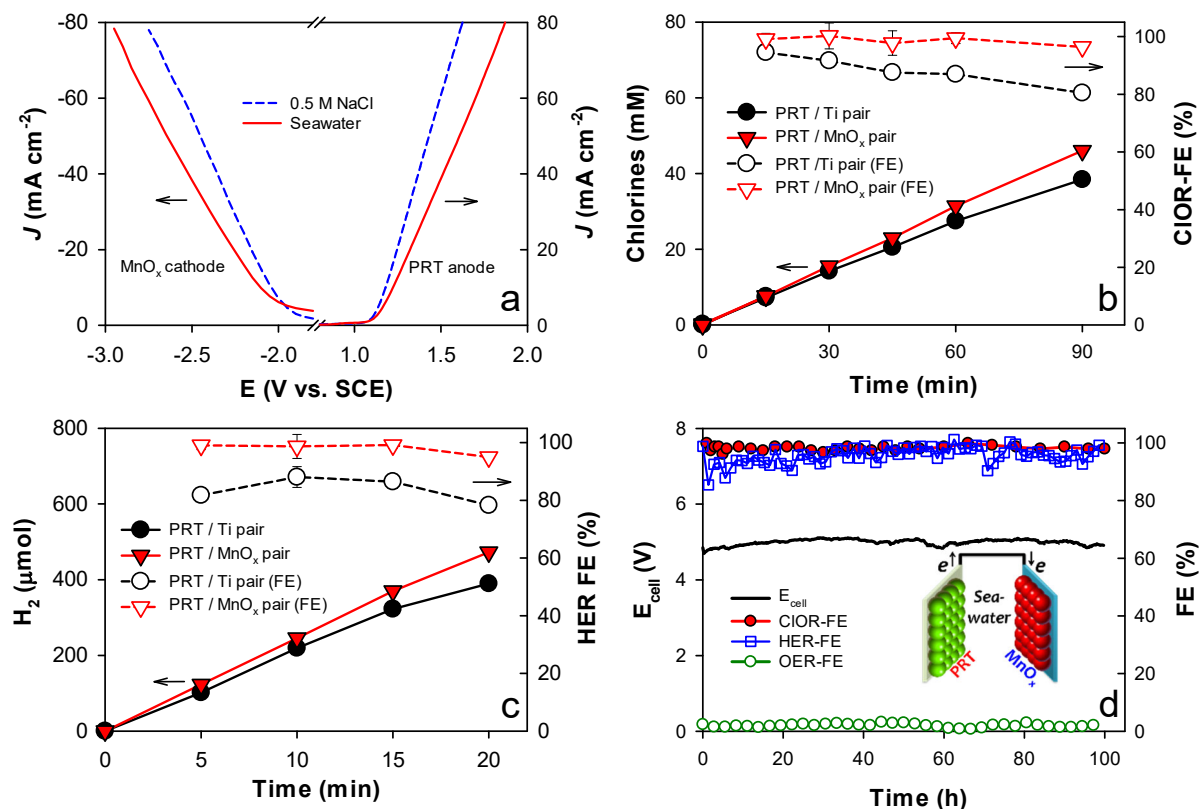

Figure 6. Seawater electrolysis with a PRT anode and MnO$_x$ cathode (PRT/MnO$_x$) pair in a single-compartment cell. (a) Linear sweep voltammograms of each electrode in 0.5 M NaCl and seawater solution (salinity 36 g L^{-1}). (b) Production of chlorines and ClOR-FEs with PRT/Ti and PRT/MnO$_x$ pairs at J_{cell} = 80 mA cm^{-2} in seawater solution. (c) Production of H$_2$ and HER-FEs with PRT/Ti and PRT/MnO$_x$ pairs at J_{cell} = 80 mA cm^{-2} in seawater solution. (d) Prolonged electrolysis with the PRT/MnO$_x$ pair at J_{cell} = 80 mA cm^{-2} in seawater solution. Evolved H$_2$ and O$_2$ gases were *in situ* real time measured while chlorines were intermittently analyzed. Changes in E_{cell} were also recorded.

Conclusions

This study successfully demonstrated the production of high-purity H_2 using a ClOR-selective anode and HER-selective cathode pair via membraneless electrolysis of undisturbed, unbuffered seawater. An optimized ternary PRT electrocatalyst with a minimized Pt level exhibited superior activity compared with single and binary component catalysts for the selective production of chlorines in saline and seawater, with complete inhibition of the OER. Such an activity can be attributed to the excellent surface and electrochemical characteristics of the PRT electrocatalyst, including a large surface area and low interfacial charge-transfer resistance. The PRT electrocatalyst maintained industry-level stability with constant ClOR activity over 500 h under severe conditions. Moreover, MnO_x drove the HER at an FE of ~100% in the presence of free chlorines while completely inhibiting the ClRR. In contrast, the ClRR and HER occurred concurrently with other commonly used electrodes (Ti and Pt), reducing the HER efficiency. The observed selectivity of the HER with MnO_x was associated with the limited interaction of free chlorines. Finally, the PRT anode/MnO_x cathode pair produced H_2 gas at an FE of ~100% via seawater electrolysis at pH 8.2 over 100 h in a membraneless reactor. No O_2 was evolved, whereas ClOR occurred at an FE of ~100% during seawater electrolysis. The as-developed electrolyzer does not require the use of membranes for producing high-purity H_2 with an FE of ~100% via unbuffered natural seawater electrolysis.

References

1   G. Kakoulaki, I. Kougias, N. Taylor, F. Dolci, J. Moya and A. Jäger-Waldau, *Energy Convers. Manag.*, 2021, **228**.

2   M. Yue, H. Lambert, E. Pahon, R. Roche, S. Jemei and D. Hissel, *Renew. Sustain. Energy Rev.*, 2021, **146**.

3   J. Ivy, *Summary of electrolytic hydrogen production: milestone completion report*, National Renewable Energy Laboratory (NREL/MP-560-36734), September 2004.

4   M. A. Khan, T. Al-Attas, S. Roy, M. M. Rahman, N. Ghaffour, V. Thangadurai, S. Larter, J. Hu, P. M. Ajayan and M. G. Kibria, *Energy Environ. Sci.*, 2021, **14**, 4831-4839.

5   M. R. Shaner, H. A. Atwater, N. S. Lewis and E. W. McFarland, *Energy Environ. Sci.*, 2016, **9**, 2354-2371.

6   H. Park, *J. Environ. Chem. Eng.*, 2022, **10**, 106919.

7   J. Kim, W. J. K. Choi, J. Choi, M. R. Hoffmann and H. Park, *Catal. Today*, 2013, **199**, 2-7.

8   H. Park, C. D. Vecitis and M. R. Hoffmann, *J. Phys. Chem. A*, 2008, **112**, 7616-7626.

9   H. Park, C. D. Vecitis, W. Choi, O. Weres and M. R. Hoffmann, *J. Phys. Chem. C*, 2008, **112**, 885-889.

10   H. Dagdougui, A. Ouammi and R. Sacile, *Int. J. Hydro. Energy*, 2011, **36**, 14324-14334.

11   A. Christensen, *Assessment of Hydrogen Production Costs from Electrolysis: United States and Europe, The International Council on Clean Transportation, June 4, 2020.*

12   I. A. Gondal, *Sustain. Energy Fuels*, 2019, **3**, 1468-1489.

13   R. d'Amore-Domenech and T. J. Leo, *ACS Sustain. Chem. Eng.*, 2019, **7**, 8006-8022.

14   S. Bolar, S. Shit, N. Chandra Murmu and T. Kuila, *Sustain. Energy Fuels*, 2021, **5**, 5915-5945.

15   S. Kim, D. S. Han and H. Park, *Appl. Catal. B*, 2021, **284**, 119745.

16   B.-j. Kim, G. Piao, S. Kim, S. Y. Yang, Y. Park, D. S. Han, H. K. Shon, M. R. Hoffmann and H. Park, *ACS Sustain. Chem. Eng.*, 2019, **7**, 15320-15328.

17   S. Kim, G. Piao, D. S. Han, H. K. Shon and H. Park, *Energy Environ. Sci.*, 2018, **11**, 344-353.

18   H. Park, A. Bak, Y. Y. Ahn, J. Choi and M. R. Hoffmannn, *J. Hazard. Mater.*, 2012, **211**, 47-54.

19   H. Park, C. D. Vecitis and M. R. Hoffmann, *J. Phys. Chem. C*, 2009, **113**, 7935-7945.

20   S. Khatun, H. Hirani and P. Roy, *J. Mater. Chem. A*, 2021, **9**, 74-86.

21   K. S. Exner, J. Anton, T. Jacob and H. Over, *Angew. Chem. Int. Edit.*, 2014, **126**, 11212-11215.

22   S. Kim, S. K. Choi, B. Y. Yoon, S. K. Lim and H. Park, *Appl. Catal. B*, 2010, **97**, 135-141.

23   Y. Y. Ahn, S. Y. Yang, C. Choi, W. Choi, S. Kim and H. Park, *Catal. Today*, 2017, **282**, 57-64.

24   B. Endrődi, A. Stojanovic, M. Cuartero, N. Simic, M. Wildlock, R. de Marco, G. A. Crespo and A. Cornell, *ACS Sustain. Chem. Eng.*, 2019, **7**, 12170-12178.

25   J. Chang, G. Wang, Z. Yang, B. Li, Q. Wang, R. Kuliiev, N. Orlovskaya, M. Gu, Y. Du, G. Wang and Y. Yang, *Adv. Mater.*, 2021, **33**, 2101425.

26   S. Dresp, F. Dionigi, M. Klingenhof and P. Strasser, *ACS Energy Lett.*, 2019, **4**, 933-942.

27   F. Dionigi, T. Reier, Z. Pawolek, M. Gliech and P. Strasser, *ChemSusChem*, 2016, **9**, 962-972.

28   S. Jiang, H. Sun, H. Wang, B. P. Ladewig and Z. Yao, *Chemosphere*, 2021, **282**, 130817.

29   M. Götz, J. Lefebvre, F. Mörs, A. McDaniel Koch, F. Graf, S. Bajohr, R. Reimert and T. Kolb, *Renew. Energy*, 2016, **85**, 1371-1390.

30   J. N. Hausmann, R. Schlögl, P. W. Menezes and M. Driess, *Energy Environ. Sci.*, 2021, **14**, 3679-3685.

31   W. L. Ang, A. W. Mohammad, N. Hilal and C. P. Leo, *Desalination*, 2015, **363**, 2-18.

32   M. Wang, B.-j. Kim, D. S. Han and H. Park, *Chem. Eng. J.*, 2021, **425**, 131435.

33   W. Choi, J. H. Choi and H. Park, *Chem. Eng. J.*, 2021, **409**, 128175.

34   S. Panigrahy, R. Samanta, P. Panda, R. Mishra and S. Barman, *Int. J. Energy Res.*, 2021, **46**, 6406-6420.

35   D. Wang, H. L. Xin, R. Hovden, H. Wang, Y. Yu, D. A. Muller, F. J. DiSalvo and H. D. Abruna, *Nat. Mater.*, 2013, **12**, 81-87.

36   J. C. Meier, I. Katsounaros, C. Galeano, H. J. Bongard, A. A. Topalov, A. Kostka, A. Karschin, F. Schüth and K. J. J. Mayrhofer, *Energy Environ. Sci.*, 2012, **5**.

37   E. S. Ilton, J. E. Post, P. J. Heaney, F. T. Ling and S. N. Kerisit, *Appl. Surf. Sci.*, 2016, **366**, 475-485.

38   J. Guo, X. Zhang, X. Du and F. Zhang, *J. Mater. Chem. A*, 2017, **5**, 6447-6454.

39   B. Endrődi, O. Diaz-Morales, U. Mattinen, M. Cuartero, A. K. Padinjarethil, N. Simic, M. Wildlock, G. A. Crespo and A. Cornell, *Electrochim. Acta*, 2020, **341**.

40   T. Watanabe, K. Akai and Y. Einaga, *Electrochem. Commun.*, 2016, **70**, 18-22.

41   K. Hedenstedt, A. S. O. Gomes, M. Busch and E. Ahlberg, *Electrocatalysis*, 2016, **7**, 326-335.

42   H. Zhang, A. Wu, H. Fu, L. Zhang, H. Liu, S. Zheng, H. Wan and Z. Xu, *RSC Adv.*, 2017, **7**, 41228.

43   L. Yu, L. Wu, B. McElhenny, S. Song, D. Luo, F. Zhang, Y. Yu, S. Chen and Z. Ren, *Energy Environ. Sci.*, 2020, **13**, 3439-3446.

Supplementary Files

This is a list of supplementary files associated with this preprint. Click to download.

- SupportingInformation.pdf